



CHAPTER II

LITERATURE REVIEW

2.1 Principles of Corrosion of Materials

2.1.1 Definition of Corrosion

Corrosion can be defined as the deterioration of material by reaction with its surroundings. Corrosion mostly refers to any process involving the deterioration or degradation of metal components. The corrosion occurs because of the natural tendency for most metals to combine chemically with elements to form compounds and return to their natural state (NASA - Corrosion Control and Treatment Manual, 2011). Most metals corrode on contact with water (and moisture in the air), acids, bases, salts, oils, aggressive metal polishes and other solid and liquid chemicals. Metals will also corrode when exposed to gaseous materials like acid vapors, formaldehyde gas, ammonia gas, and sulfur containing gases (NACE Resource Center - Corrosion Theory, 2011).

The consequences of corrosion are many; for example: the loss of mechanical strength and structural integrity, personal hazards or injuries and environmental contamination. These effects can cause added complexity and expense of equipment, which needs to be designed to resist a certain amount of corrosion and to allow corroded components to be conveniently replaced.

In engineering design, corrosion protection plays an important role. The aim of active corrosion protection is to influence the reactions that proceed during corrosion, it being possible to control not only temperature, pressure and corrosive agent but also the reaction itself in such a manner that corrosion is avoided.

2.1.2 Types of Corrosion

There is no exact total for the number of corrosion types. However, most corrosion experts can agree on the basic varieties of corrosion as in the table below (Table 2.1).

Table 2.1 Types of corrosion (Grundke,1976)

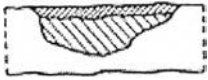


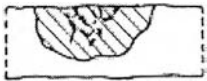

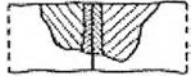


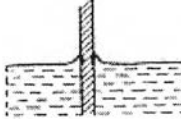
 <p>Uniform corrosion</p> <p>The reaction starts at the surface and proceeds uniformly.</p>	 <p>Localized corrosion (pitting corrosion)</p> <p>The base metal is eaten away and perforated in places in the manner of holes.</p>	 <p>Wide pitting corrosion</p> <p>The corrosion causes localized scarring or wastage.</p>
 <p>Intergranular corrosion</p> <p>Imperceptible or barely perceptible from outside, since the corrosion proceeds at the grain boundaries.</p>	 <p>Transgranular or intragranular corrosion</p> <p>The grain boundary material is retained, since the corrosion proceeds preferentially within the grain.</p>	 <p>Galvanic corrosion</p> <p>Increased corrosion in cracks or at contact surfaces between components of different metals.</p>

Table 2.1 (Cont'd) Types of corrosion (Grundke, 1976)

 <p>Selective corrosion</p> <p>Corrosive attack on structural components.</p>	 <p>Exfoliation corrosion</p> <p>Corrosion follows "fiber orientation".</p>	 <p>Interfacial corrosion</p> <p>Frequently observed at water-air interfaces.</p>
---	---	---

2.2 Physical Methods Investigation

2.2.1 Fundamental Principles of Scanning Electron Microscopy (SEM)

The Scanning Electron Microscope (SEM) uses a focused beam of high-energy electrons to generate a variety of signals at the surface of solid specimens. The signals that derive from electron-sample interactions show information about the sample, including external morphology or texture, chemical composition, and crystalline structure and orientation of materials making up the sample.

The SEM is also capable of performing analyses of selected point locations on the sample; this approach is especially useful in qualitatively or semi-quantitatively determining chemical compositions, crystalline structure, and crystal orientations (Swapp, 2011).

Accelerated electrons in SEM carry significant amounts of kinetic energy and this energy is dissipated as a variety of signals produced by electron-sample interactions when the incident electrons are decelerated in the solid sample.

These signals include secondary electrons (that produce SEM images), backscattered electrons (BSE), diffracted backscattered electrons (EBSD that are used to determine crystal structures and orientations of minerals), photons (characteristic X-rays that are used for elemental analysis and continuum X-rays),

visible light (cathodoluminescence-CL) and heat. Secondary electrons and backscattered electrons are commonly used for imaging samples: secondary electrons are most valuable for showing morphology and topography on samples and backscattered electrons are most valuable for illustrating contrasts in composition in multiphase samples (Swapp, 2011).

In conjunction with Scanning Electron Microscopy (SEM), Energy Dispersive X-ray Analysis (EDX) technique is used for performing chemical analysis or material composition and is not a true surface science technique, producing signals down to one μm or so below the sample surface. The analytical data are in the form of spectra, viewed during accumulation on a computer monitor, which display the number of X-rays detected as a function of the X-ray energy. An electron beam strikes the surface of a conducting sample (SEM). This causes X-rays to be emitted from the irradiated material. A two-dimensional image of each element in the sample can be acquired by moving the electron beam across the material. Due to the low X-ray intensity, images usually take a number of hours to be acquired. Elements of low atomic number are difficult to detect by EDX (GlobalSino, 2011).

2.2.2 Fundamental Principles of Dial Indicator

Dial indicators (dial gauges and probe indicators) are instruments used to measure small linear distances accurately. They are normally used in industrial and mechanical processes.

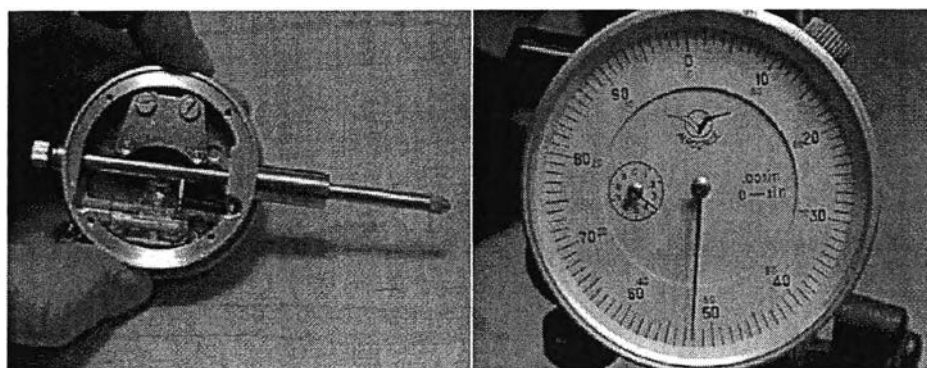


Figure 2.1 Dial inspector (Edward J. Bennett Company, 2005).

Inside the dial gauge, there is a simple rack and pinion gear system. The rack is connected to the plunger and the pinion gear is connected through a series of other gears to the dial pointer. The spring loading on the plunger is part of a mechanism that counteracts play and backlash in this gearing system. Dial indicators are almost never used to measure extended distances. Most often they are used to measure small changes in distance. The dial indicator is used by placing the stylus of the dial indicator against an object and rotating the scale by setting the zero point as a reference point. If the object or the indicator moves, the pointer on the dial will move from that reference point for indicating the change in distance (Edward J. Bennett Company, 2005).

2.3 Flow Accelerated Corrosion (FAC)

Flow-accelerated corrosion can occur in all types of nuclear units, fossil-fired units, and industrial steam systems. Flow-accelerated corrosion (FAC) is the action of corrosion and erosion in the presence of a moving fluid (liquid water or wet steam). The resulting FAC results in loss of material and reduction of wall thickness.

Under the specific conditions of FAC, the oxide layer that protects the metal underneath becomes thinner. This situation increases the corrosion rate with the consequent decrease of component wall thickness. Experimental evidence suggests that the characteristics of the flow and the mass transfer play a major role in determining the corrosion rate and the corrosion location. FAC risks can be reduced by improved designs, better choice of materials and optimization of plant cycle (Zinemanas and Herszage, 2008).

As a fundamental contributor to FAC, solubility of oxides results in thinning and is strongly influenced by fluid velocity, water chemistry, temperature, piping configuration and alloy content. This type of flow-assisted acceleration in dissolution occurs in single-phase FAC. This is primarily a corrosion process enhanced by electro-chemical dissolution and mass transfer, rather than a mechanical process. This is an extension of the general carbon steel corrosion process in stagnant water. The situation is aggravated when there is enhanced turbulence (e.g. downstream of flow meters causing flow limitation), which increases the flow rate at localized

regions. Optimizing operating parameters can help in minimizing the FAC (Kain et al., 2008).

Corrosive conditions along the flow path and mass transfer coefficients at the structure surface can be calculated to identify high FAC risk zones. Then, wall thinning rates are calculated with a coupled model of static electrochemical analysis and dynamic double oxide layer analysis. Figure 2.2 shows parameters overlapping to form a high FAC risk zone. The necessary conditions for FAC are designated as overlapping conditions of each FAC risk zone. In addition, controlling each parameter so that it stays outside the FAC risk zone can mitigate FAC (Koshizuka et al., 2010 and Naitoh et al., 2008).

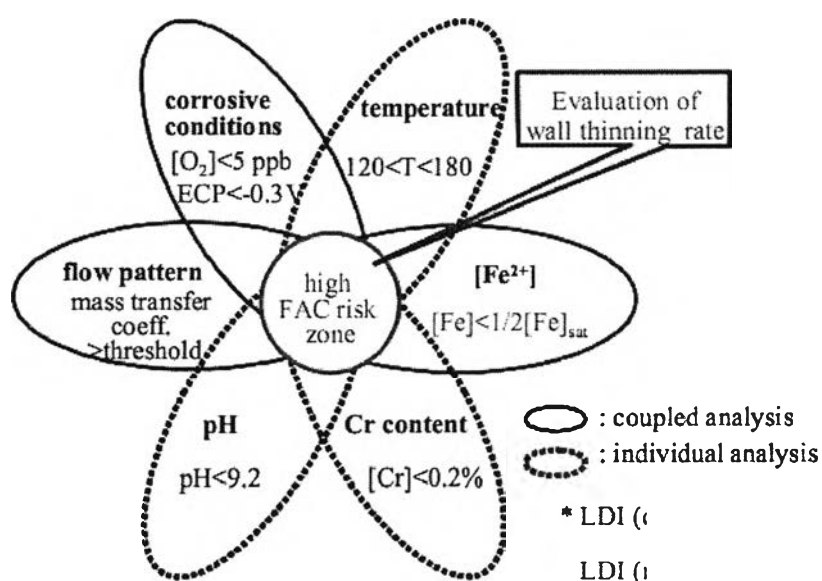


Figure 2.2 FAC risk zone (Koshizuka et al., 2010 and Naitoh et al., 2008).

Experiments on the FAC of carbon steel have been carried out using on-line electrical resistance probes installed in series in a laboratory loop operating under simulated Light Water Reactor (LWR) feed-water conditions. Under neutral conditions FAC was controlled by mass transfer, and correlations were formulated. Under ammoniated chemistry, lower FAC rates were measured – attributed to the lower solubility and slower dissolution of the magnetite film. The stifling of FAC by added oxygen occurred at higher concentrations in neutral water (Lister et al., 2008).

Nasrazadani et al. (2009) found in investigations of extraction pipes that the morphology of scallops (dimples or texturing of the surface in FAC) was dominant with severe pitting at regions where excessive wall thinning was observed, and few bands observed, indicating flow was single-phase. Highly-crystallized maghemite and lepidocrocite were detected in almost all pipes.

The geometry of each piping component and the temperature of the fluid play a major role on the rate of FAC. FAC is induced by chemical, physical and hydrodynamic factors. Other variables that effect FAC are material composition, flow velocity and turbulence and water and steam chemistry. For these reasons, it is necessary to understand and model the FAC mechanism.

2.4 Oxide Film

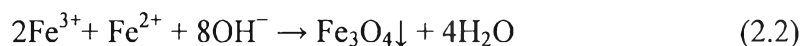
The oxide film on structure surfaces is the key factor determining FAC; it develops as a result of corrosion and controls the corrosion rate. Dissolution in turbulent coolant can cause the protective magnetite film's being thinner, so that it reaches a steady-state thickness at a constant FAC. Therefore, increases in the flow increase the mass transport due to a decrease in the boundary layer thickness (Lister et al., 2008).

When reaction with dissolved oxygen is involved, it has to enter through the pores of the oxide (magnetite) on carbon steel to the metal-oxide interface, where it must react with the Fe^{2+} ions as they are produced and eventually form a more protective oxide based on Fe_2O_3 (maghaemite or haematite) rather than Fe_3O_4 (magnetite). In diffusing through the magnetite, it will also react with the Fe^{2+} in the oxide surface and may never reach the metal if the driving force (concentration in the coolant) is too low. On the other hand, when a surface is stifled with a passive metal-oxide interface protected with Fe_2O_3 and the coolant becomes reduced in oxygen, the oxide has to be reduced to some extent before the production of Fe^{2+} ions can recommence at the metal surface (Lister et al., 2008).

The interesting magnetic properties of Fe_3O_4 have important applications in pigments (Zakaria, 2004), recording materials, photocatalysis, ferro-fluid technology

and magnetic refrigeration. Fe_3O_4 in thin film form has been attracting extensive research interest due to its application in modern magnetic devices.

The possible chemical mechanism for the hydrothermal formation of the Fe_3O_4 films can be expressed as equations 2.1 and 2.2.



Zhu et al. (2006) studied hydrothermal growth and characterization of magnetite (Fe_3O_4) thin films by using hydrazine hydrate ($\text{N}_2\text{H}_4 \cdot \text{H}_2\text{O}$) as the mineralizer to synthesize oxide nanostructures. Hydrazine is an inorganic compound (N_2H_4). It is a colourless flammable liquid. Hydrazine is highly toxic and dangerously unstable unless handled in solution. Hydrazine hydrate and $\text{FeSO}_4 \cdot 7\text{H}_2\text{O}$ were added to deionized water with stirring for forming colloid solution in an autoclave. Then, a nickel substrate (1 cm in diameter) was put into the autoclave at 150 °C for 8 h. In Figure 2.3, the Fe_3O_4 grains near the external surface ($\sim 1 \mu\text{m}$) are bigger than those grains near the interface. In the solution, submicron Fe_3O_4 particles ($\sim 200 \text{ nm}$) remaining were found. Hydrothermal methods of synthesis provoke much interest due to their operational simplicity, cost-effectiveness and capability for large-scale production. Fe_3O_4 nanoparticles have been synthesized by this hydrothermal process using hydrazine hydrate as the mineralizer. Ni (II) and Co (II) can be reduced by hydrazine directly in either water or ethanol, whereas surface catalysis or high pressure induction needs to be used for the reduction of Fe (III) and Fe (II) in the reaction mixture to avoid the kinetic difficulty.

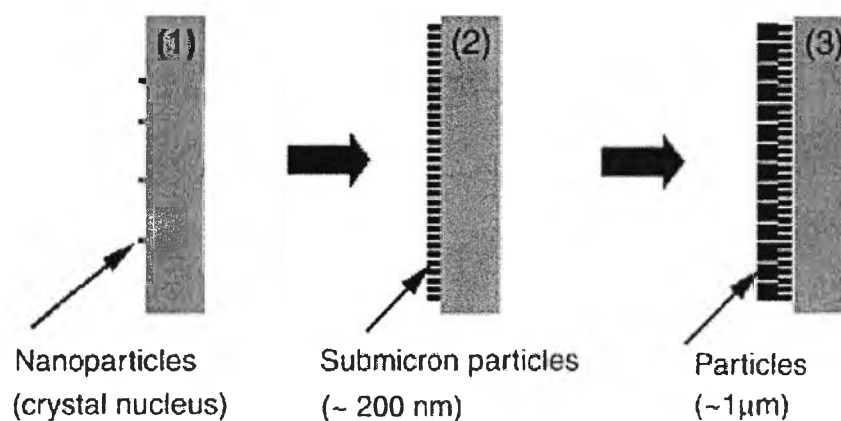
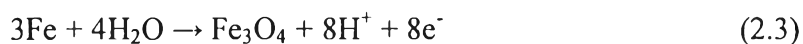


Figure 2.3 Sketch of the growth mechanism of the Fe_3O_4 film (Zhu et al., 2006).

During the first stage, Fe_3O_4 crystal nuclei (nanoparticles) were increasingly formed on the surface of the nickel substrate. Next, the crystal nuclei grew and the first layer composed of particles size 200 nm was formed. In addition, the particles in this layer clearly showed a preferred orientation along the direction vertical to the substrate. Finally, some of the submicron particles on the exterior surface began to grow, and the second layers composed of the Fe_3O_4 particles of 1 μm were formed (Zhu et al., 2006).

Cheng and Steward (2004) studied the corrosion of carbon steels in high-temperature water by using electrochemical techniques. They found that the growth of the oxide layer on steel in high-temperature water occurs by the outward diffusion of iron ions. Iron dissolution occurs where no oxide layer exists. Firstly, iron ions are generated by the anodic dissolution reaction of steel. The anodic dissolution reaction drives the important species transported through the oxide layer. Water molecules diffuse through the inner oxide layer and react directly with steel at the steel/oxide interface. Protons at the oxide/water interface diffuse through the oxide layer under the concentration and potential gradients and discharge as hydrogen atoms at the steel/oxide interface. The relevant reactions occurring at the steel/oxide interface are





The ferrous ions diffusing out of the oxide layer exist as $\text{Fe}(\text{OH})^+$ in high temperature water; they must stabilize themselves by decreasing their charge/radius ratio through hydrolysis to form hydrous iron ions. The hydrous iron ions will deposit as loose $\text{Fe}(\text{OH})_2$ once the saturation of iron ions is achieved. The outer deposition of the magnetite layer is then formed in high-temperature water, accompanying the discharge of hydrogen ions. Therefore, the electrochemical reactions occurring at the oxide/water interface are



It is convenient to consider the corrosion processes of steel as the simultaneous formation of two molecules of Fe_3O_4 , one at the steel/oxide interface, and the other at the oxide/water interface. The formation of an Fe_3O_4 film on a steel surface reduces the dissolution rate of the steel substantially (Cheng and Steward, 2004).

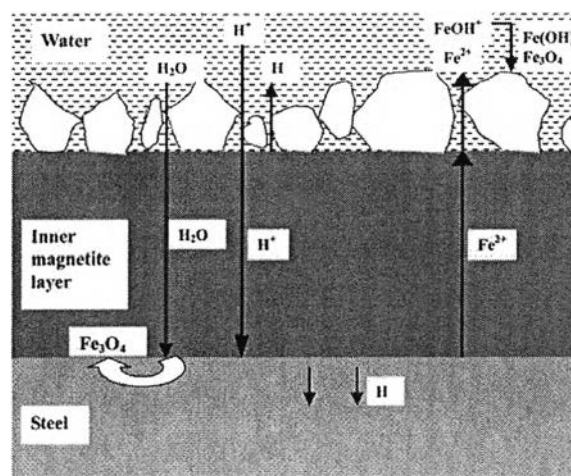


Figure 2.4 A schematic view of the formation mechanism of the magnetite film on the steel surface in high temperature water (Cheng and Steward, 2004).

Metallic ions (Fe^{2+}) are released into the water at the boundary layer where some of the supersaturated Fe^{2+} ions become oxide particles and deposit on the metal surface to become a magnetite oxide layer. The oxide layer plays an important role in preventing corrosion reaction. The flow dynamics affect the thickness of the boundary layer. In addition, oxygen concentration in the boundary layer also plays an important role for oxidizing magnetite to hematite, which contributes to achieving much higher corrosion resistance. Temperature and pH of water are also important environmental factors to determine FAC. Ferrous ion concentration in the water is calculated with a chemical reaction model based on the obtained flow pattern, and then fed back to the environmental factors for the wall thinning calculation (Koshizuka et al., 2010).

2.5 Scalloped Surface

Surfaces corroded by FAC develop thin magnetite films overlaying typical “scalloped” textures. Scallops are influenced by the microscopic oxide structures that developed from underlying metal grains; in particular, under feed water conditions, pearlite grains formed lamellar oxides that predominated on scallop crests (Lister et al., 2008).

The passive-bed theory of erosional marks assumes that the characteristics of the marks are determined by the fluid dynamics in contact with the surface. The properties of the material have therefore no influence on the formation of the scallops. The length of the erosion marks is assumed constant with time. Sharp (1974) and Leighly (1948) proposed that the characteristics of scallops on ice surfaces were controlled by the properties of vortices in the adjacent air. Henderson and Perry (1958) and Curl (1974) support the same idea with studies of meteorites and limestone caves, respectively.

The defect theory affirms that the position of each erosional mark is due to the initial presence of an irregularity or a defect at the surface. It assumes an independent evolution for each mark and an increase of length and amplitude with time up to a limit set by the initial spacing of defects. Therefore, the characteristics of any assemblage of erosional marks depend on the duration of the eroding process,

the spatial distribution, shape and dimensions of the defects and the character of the flow.

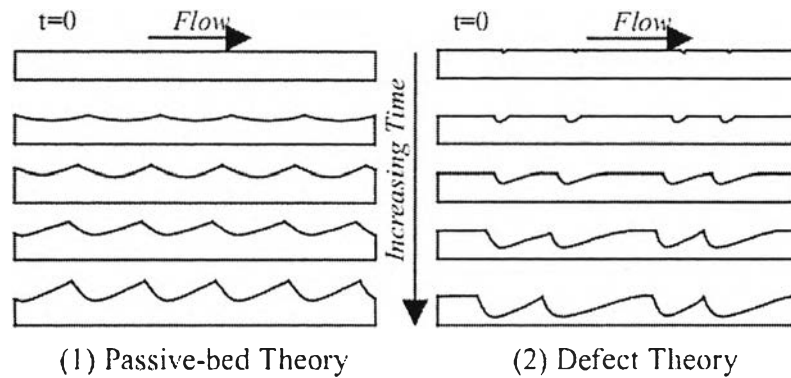


Figure 2.5 Evolution of a surface according to (1) Passive-bed Theory and (2) Defect Theory (Villien et al., 2001).

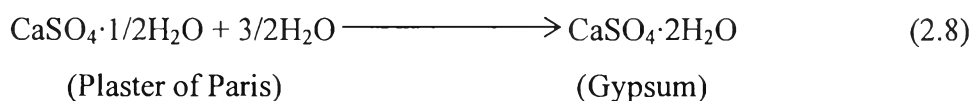
However, the very development of the corresponding morphological structures on the wall surface (scallops and flutes) becomes an extremely complex task from the turbulence modeling point of view. Clearly, the dissolution behavior of the surface is key to the formation of scallops, and is the subject of several research projects at UNB Nuclear that are investigating the basic phenomena of corrosion of steel in water. This thesis examines the characteristics of the apparatus used for studying oxide dissolution.

2.6 Plaster of Paris ($\text{CaSO}_4 \cdot 1/2\text{H}_2\text{O}$)

Unhydrated plaster of Paris is calcium sulfate hemihydrate ($\text{CaSO}_4 \cdot 1/2\text{H}_2\text{O}$), having purity of not less than 95% $\text{CaSO}_4 \cdot 1/2\text{H}_2\text{O}$ by mass. It consists of calcined gypsum with small amounts of additives (less than 5% by mass) to modify physical characteristics. To produce a plaster, slurry can be formed to the desired shape and will set to a hard and rigid structure. It is a generic name for a family of powdered cementitious products consisting primarily of calcined gypsum with additives to modify physical characteristics, and having the ability, when mixed with water and aggregate, to produce a plastic mortar or slurry which can be formed

to the desired shape by various methods and will subsequently set to a hard and rigid substance.

Plaster of Paris will be chosen as the substrate for many dissolution experiments as it presents many advantages. For example, plaster of Paris is easily cast to suitable size and shape, furthermore it is inexpensive and replacement of the test section can be easily made. In addition, the solubility of the plaster in water is reasonable and significant results can be obtained in a short period of time. When plaster is mixed with water, a reaction takes place and water is absorbed by the calcium sulfate hemihydrate to form the dihydrate generally referred to as gypsum, as in equation 2.8.



2.7 Gypsum Crystal Characteristics

Gypsum is found in nature in common rock and mineral form. The chemical formula of gypsum is $\text{CaSO}_4 \cdot 2\text{H}_2\text{O}$ (calcium sulfate). Gypsum is a sedimentary rock and a mineral, it can form extremely large crystals. Crystals of gypsum can be colorless and transparent, making a strong contrast to the compressed powder as the most common usage in drywall. Gypsum is a natural insulator, feeling warm to the touch when compared to many other rocks or quartz crystals. Sheets of clear crystals can be easily peeled from a larger specimen (Amethyst Galleries, Inc., 2011). The physico-chemical characteristics of gypsum are summarized in Table 2.2.

Table 2.2 Physico-chemical characteristics of gypsum (Amethyst Galleries, Inc., 2011, Wallace A. G., 2003 and Gypsum in Handbook of Mineralogy, 2005).

Category	Sulfate mineral
Color	Usually white, colorless or gray
Transparency	Transparent to translucent
Tenacity	Flexible, inelastic
Luster	Pearly
Mohs scale hardness	2
Specific gravity	2.31–2.33
Molecular weight (g/mol)	172.171
Density (g/cm ³)	2.32
Solubility in water at 25°C (g/L)	2.205
Mass diffusivity in water at 25°C (m ² /s)	9.084E-10

2.8 Dissolution Rate of Crystal of Gypsum and Plaster of Paris

The dissolution rate of a solid into an aqueous solution is controlled by the chemical reaction at the surface or by molecular diffusion through the boundary layer. In both cases, rate of solute transport through the boundary layer, at steady state, will be equal to the mass flow of the dissolved material at the surface.

Most of the studies of the dissolution of gypsum have been made with hydrated plaster of Paris (CaSO₄·2H₂O). Villien et al. (2001) found that when the diffusion transfer is high enough to ensure that the surface concentration of the dissolved species is close to that in the bulk flow, the rate of dissolution is controlled by the reaction rate at the surface. On the other hand, when the diffusion transfer is relatively low and/or the dissolution rate at the surface is high, molecular diffusion becomes the limiting step. An increase in the fluid velocity will enhance mass transfer.

Early studies (Liu and Nancollas, 1971, James and Lupton, 1978, Opdyke et al., 1987) showed that the dissolution kinetics are generally transport-controlled and a first-order rate equation for dissolution rate is often proposed.

$$R = k_t \cdot (C_s - C_b) \quad (2.9)$$

$$\text{where:} \quad k_t = \frac{D}{\delta} \quad (2.10)$$

From equations 2.9 and 2.10, R is the overall dissolution rate, C_s is the concentration at the surface, C_b is the concentration of dissolved species in the bulk, k_t is the mass transfer coefficient, D is the diffusion coefficient through the boundary layer and δ is the diffusion layer thickness. This has been confirmed by the observed dependence of overall dissolution rate on the diffusion layer thickness. The higher dissolution rate is represented for a thinning of layer. Increasing the fluid velocity will decrease the thickness of the boundary layer and make the concentration gradient in the boundary layer steeper.

Rains and Dewers (1997) studied the dissolution of fine gypsum particles in mixed flow reactors, It was similar to the study of Jeschke et al., using a closed, stirred vessel instead of a mixed flow reactor. They argued that the dissolution of gypsum is jointly controlled by the surface reaction and the diffusion transport through the diffusion layer. The effective gypsum dissolution rate is then determined by “mixed” kinetics. They assumed a second order expression to describe the surface rate as equation 2.11.

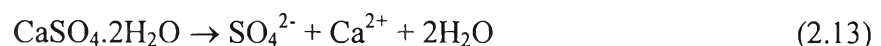
$$R = k_t \left(1 - \Omega^{1/2} + \zeta \left[1 - \left\{ 1 + \frac{2 \cdot (1 - \Omega^{1/2})}{\zeta} \right\}^{1/2} \right] \right) \quad (2.11)$$

where k_t is the transport coefficient for purely transport control, ζ is the transport reaction factor and $\Omega = C_b/C_s$. The factor ζ measures the relative influence of transport and reaction processes and is expressed as:

$$\zeta = \frac{Dm_{eq}}{2\delta k_t} \quad (2.12)$$

where m_{eq} is the molal equilibrium concentration.

Raines and Dewers (1997) suggested that there is a five-step process to chemically interact minerals with moving fluids. First, reactants in the fluid must cross a hydrodynamic boundary layer to reach the mineral surface. Second, reactants must be adsorbed onto the mineral surface. Third, a chemical reaction must take place. Fourth, products must be formed and released from the surface. Finally, the products must be transferred across the hydrodynamic boundary layer and into the bulk solution. For the case of the gypsum-water system (Equation 2.13), the reactants are H_2O and $CaSO_4 \cdot 2H_2O$ and the product are Ca^{2+} and SO_4^{2-} ions.



Villien et al.. (2005) studied the dissolution rate of plaster of Paris with four different liquid flow rates and found that when the concentration of Ca^{2+} increased, the dissolution rate of gypsum decreased approximately exponentially. The gypsum dissolution is under mixed transport/reaction control, where the transport-controlled kinetics dominate the initial dissolution and the surface reaction kinetics become more important later, which is in agreement with Raines and Dewers, (1997). The results show that a second-order reaction was better to describe the kinetics of dissolution for gypsum, but the result of second-order (Equation 2.11) showed that it seems to overestimate the dissolution rate as the solution approaches saturation.

Raines and Dewers (1997) found different characteristics of calcium sulfate caused by different amounts of impurity and porosity. They compared the dissolution rate between gypsum ($CaSO_4 \cdot 2H_2O$) and anhydrite ($CaSO_4$) samples. Anhydrite is a mineral anhydrous calcium sulfate, $CaSO_4$. From their results, the gypsum dissolved faster than anhydrite, when the steady state was achieved after four hours.

Sinthupphan (2008) and Warunphaisal (2009) studied the formation of scallops on the dissolving surface of a gypsum pipe. They observed that scallops

developed very fast at the beginning of the test and there was a strong effect on surface roughness and concentration of gypsum pipe, confirming the Defect theory.

Shao (2006) suggested that a higher driving force for mass transfer exists in a beginning of a test, and this was reduced when the concentrations of Ca^{2+} and SO_4^{2-} increased. He also found that the inlet and outlet for fluid flow in a plaster of Paris pipe had different scalloping types, which suggested that the scalloping profile is related to the dissolution rate and that higher turbulence within the entrance length may induce higher dissolution.

Azimi et al. (2007) studied the modelling of gypsum crystal solubility in concentrated multi-component sulfate solutions. They used OLI software and a mixed-solvent-electrolyte (MSE) model to find the solubility of gypsum, as shown in Figure 2.6.

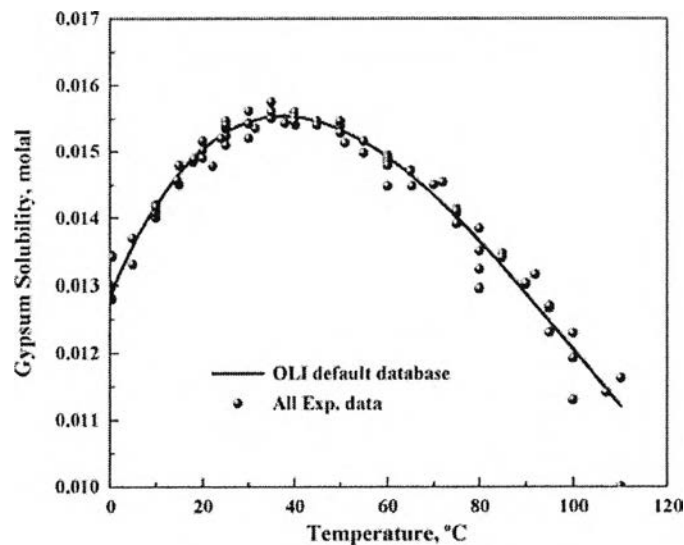


Figure 2.6 Dihydrate solubility in H_2O vs. temperature (Azimi et al.,2007).

Colombani and Bert (2007) studied the dissolution and diffusion of gypsum in pure water at ambient temperature and pressure. They found an interdiffusion coefficient $D = (1.0 \pm 0.1) \times 10^{-9} \text{ m}^2\text{s}^{-1}$ and a dissolution rate constant $k = (4 \pm 1) \times 10^{-5} \text{ mol m}^{-2}\text{s}^{-1}$. They suggested that if mass transport proceeds quickly compared to the reaction rate, the kinetics are reaction-controlled. Conversely, if mass transport is

slow compared to the chemical reaction at the solid surface, ions are rapidly unbound from the solid but slowly transported away in the solution, hence the dissolution kinetics is controlled by molecular diffusion. They evaluated dissolution velocity by an empirical dissolution rate constant, k_s and a transport constant, k_t . They found that k_s was $1.5 \times 10^{-3} \text{ mol m}^{-2} \text{ s}^{-1}$ and k_t was $1.3 \times 10^{-3} \text{ mol m}^{-2} \text{ s}^{-1}$. These two values are close enough that the mixed aspect of the dissolution kinetics is unambiguously assessed for their situation.

2.8.1 The Effect of Temperature on Dissolution of Crystal of Gypsum and Plaster of Paris Pipe

Lebedev and Lekhov (1989) studied the dissolution kinetics of gypsum crystals in water at 5-25 °C and found that the temperature dependence of the rate constant fits an Arrhenius equation. The activation energy of 10-11 kcal/mol appears to correspond to mass transfer. In addition, the rate constant seems to be proportional to the temperature. Liu and Nacollas (1971) also analysed the rate constant with an Arrhenius equation at temperature between 10 °C and 30 °C. The activation energy was 10 ± 1.5 kcal/mole, which is larger than the value of 4.5 kcal/mole to be expected on the basis of pure mass-transport control, for which only the temperature dependence of the diffusion coefficient should be important. Although much of the evidence points to diffusion across the liquid boundary layer as being the rate-controlling step in the dissolution of gypsum crystal, it is not possible in the light of this relatively large activation energy. It must be a more complicated mechanism.

Warunphaisal (2009) found that the population of scallops in a plaster of Paris pipe decreased with decreasing temperature while the dissolution rate also decreased. The dissolution rate at high temperature was more uneven than at low temperature. The uneven dissolution rate may have been caused by effect of additional sand grain impurities. However, low temperatures showed less variation than high temperatures, as shown in Figure 2.7.

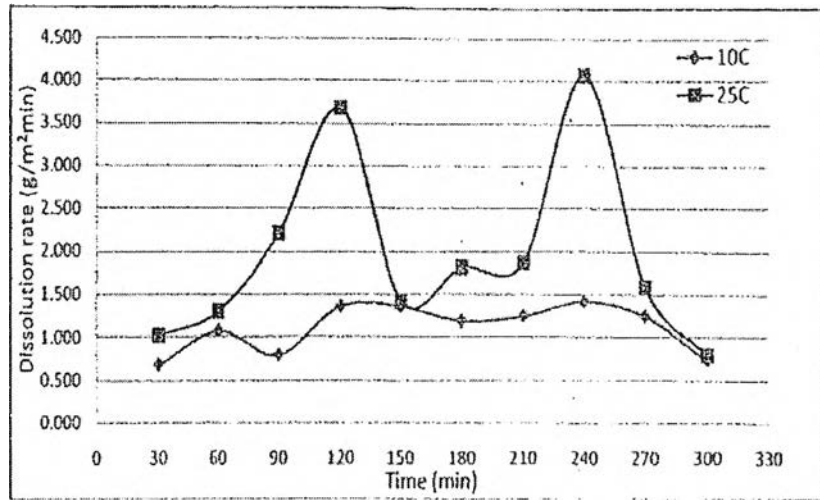


Figure 2.7 Dissolution rate on plaster of Paris pipe with time at different temperatures, 0.21-0.25 mm, 50 defects/cm³ and 25 LPM. (Warunphaisal, 2009).

2.8.2 Pressure Drop

Shao (2006) studied the effect of scalloping of difference types of plaster of Paris on pressure drop in feed water piping system. He found that the pressure drop increased at the beginning and became stable for first run but for a second run decreased as shown in Figure 2.8.

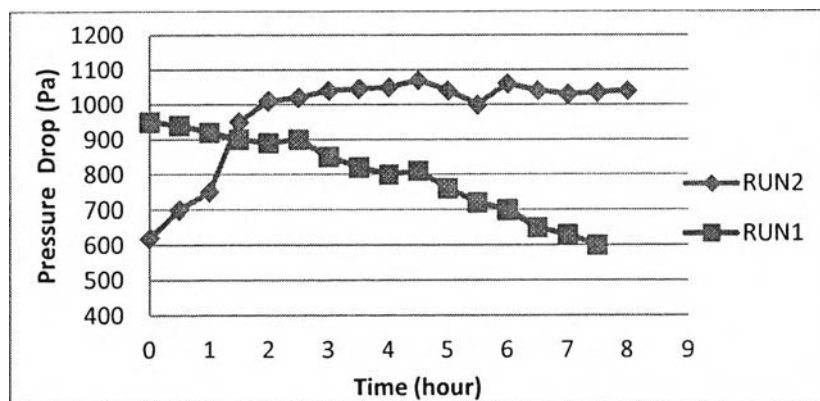


Figure 2.8 The pressure drop versus time (Shao, 2006).

The two runs operated at the same conditions but had different types of plaster of Paris (before hydration); Run1 was a pure plaster of Paris (98%

CaSO₄·1/2H₂O) and Run 2 was a commercial plaster of Paris containing impurities such as sand. The result showed that Run 2 gave high scalloping but less resistance to flow. It appears that hydrodynamic forces could make the plaster surface less resistant to flow; however, the difference between Run 1 and Run 2 was not fully explained. Shao proposed that if the scalloping can make the surface smoother, a scalloped surface could be the best choice to give the highest ratio of k/f for given roughness height, where k is mass transfer coefficient and f is friction factor. This ratio can make the scallop the desired choice for high mass transfer with low pressure drop.

Lertsurasakda (2007) investigated the effect of scallop distribution on pressure drop in water flow using tubular sections of machined acrylic plastic. He found that the pressure drop of a scalloped surface depends on the scallop surface area and is almost unaffected by the scallop distribution. He also studied the effect on pressure drop of scallop surface area with forward and backward flow. He found that the friction factors obtained from forward and backward flow are not the same, even though they have the same roughness height. The friction factors calculated from the experiment are not equal to those calculated from the Von Karman equation for fully rough surfaces in turbulent flow, which give a constant value of the friction at high Reynolds numbers.

Warunphaisal (2009) studied the effect of pressure drop of plaster of Paris pipe at two flow rates by using a differential pressure transducer. He found that pressure drop and flow rate were dependent on each other. The higher pressure drop was produced at higher flow rate (Figure 2.9). According to Fanning's equation (equation 2.14):

$$P_1 - P_2 = (2f\rho v^2) \cdot (L_1 - L_2)_p / D_p \quad (2.14)$$

where $P_1 - P_2$ is pressure drop (Pa), f is friction factor, ρ is fluid density of fluid (kg/m^3), v is flow velocity, $(L_1 - L_2)_p$ is length of pipe (m) and D_p is pipe diameter (m).

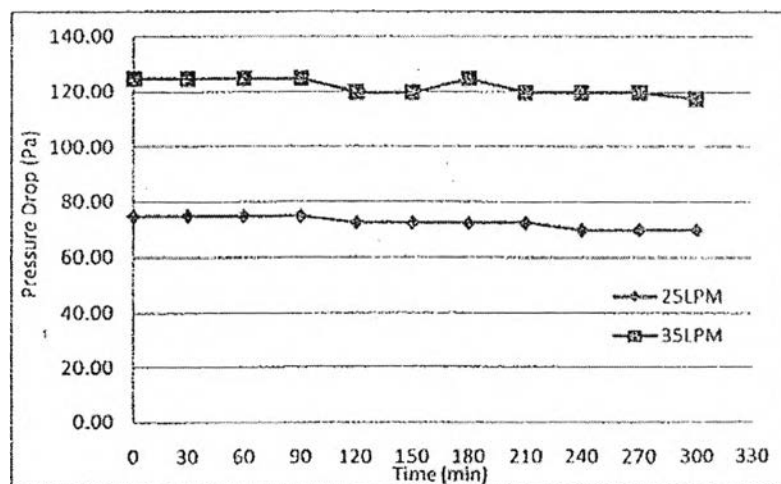


Figure 2.9 Pressure drop with time at pH3, 30°C (Warunphaisal, 2009).

2.8.3 The Effect of pH

Rechenberg and Sprung (1983) found how the solubility of calcium sulfate depends on alkali hydroxide concentration. In comparison with equilibrium curve II (Figure 2.10) on pure calcium hydroxide solutions, a higher calcium ion concentration always occurs in the presence of sulfate (equilibrium I) with the same OH^- concentration. This is due to the fact that the added sodium sulfate first reacts with calcium hydroxide forming sodium hydroxide and gypsum, and the potassium sulfate reacts forming potassium hydroxide and gypsum or syngenite ($\text{K}_2\text{Ca}(\text{SO}_4)_2 \cdot \text{H}_2\text{O}$) which are less soluble in these conditions than the calcium hydroxide. In the precipitate of the equilibrium solution, in addition to calcium hydroxide, gypsum and syngenite are identified by means of a differential scanning calorimeter (DSC). The course of the two equilibrium curves shows that in contrast to solutions without sulfate the OH^- concentration also influences the Ca^{+2} concentration in solutions containing sulfate as (shown in Figure 2.10).

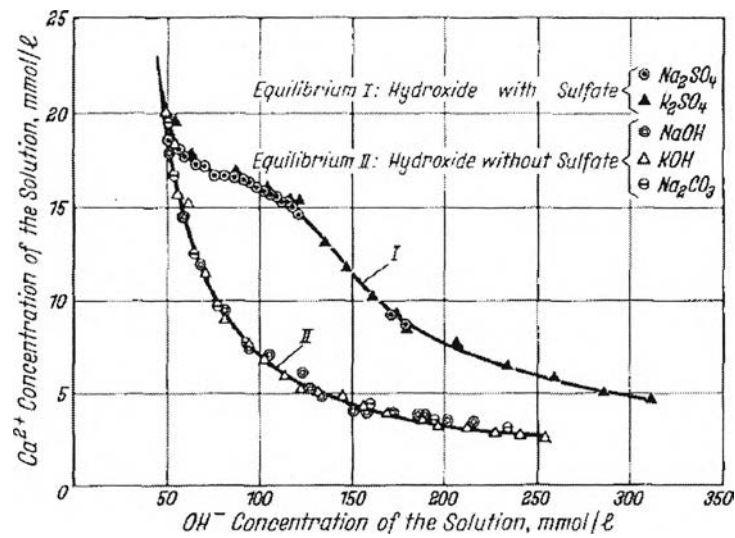


Figure 2.10 Dependence of Ca^{2+} concentration on the OH^- concentration in the solution with and without sulfate (Rachenberg and Sprung, 1983).

Azimi et al. (2007) found that the solubility of gypsum hydrate in H_2SO_4 solution at low temperature ($25\text{-}60^\circ\text{C}$) increased and then decreased moderately with increases in H_2SO_4 .

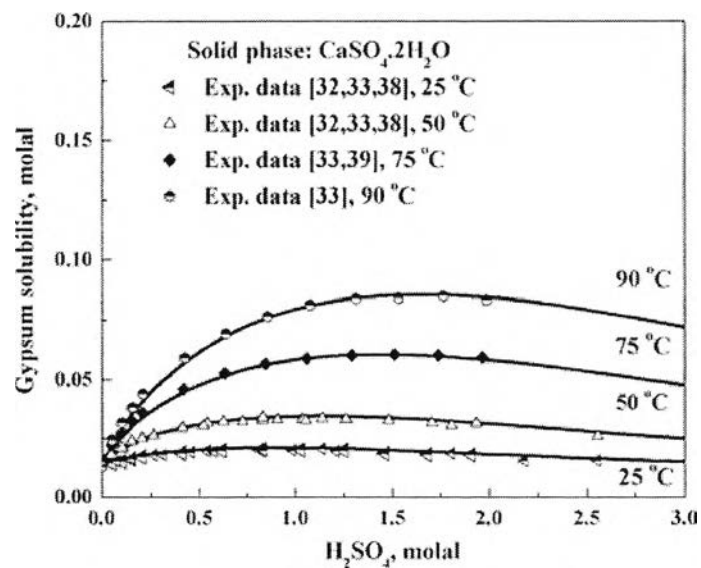


Figure 2.11 Gypsum solubility in H_2SO_4 solutions at different temperatures (Azimi, 2007).

Sinthuphan (2008) found that the population of scallops on dissolving plaster of Paris pipe is reduced by increasing pH. The dissolution rate increases slightly with time in acid and neutral solutions but decreases initially before stabilizing in a basic solution, as shown in Figure 2.12.

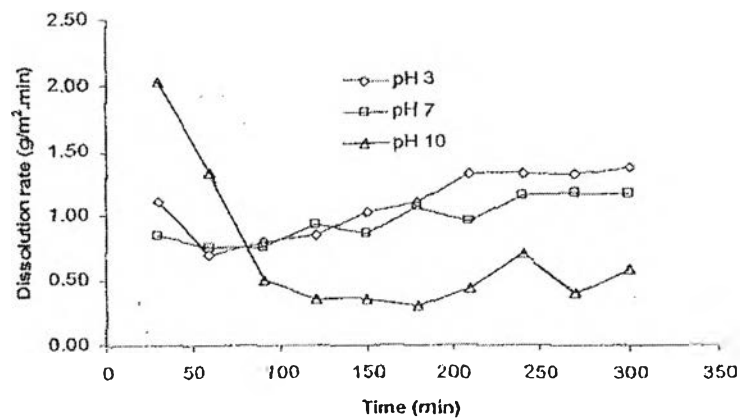


Figure 2.12 Comparison of dissolution rates at difference pHs (Sinthuphan, 2008)

Warunphaisal (2009) measured the dissolution rates in solution of different pH along a plaster pipe with no defects, as shown in Figure 2.13. The result showed that the dissolution rate followed the same trend at different pHs.

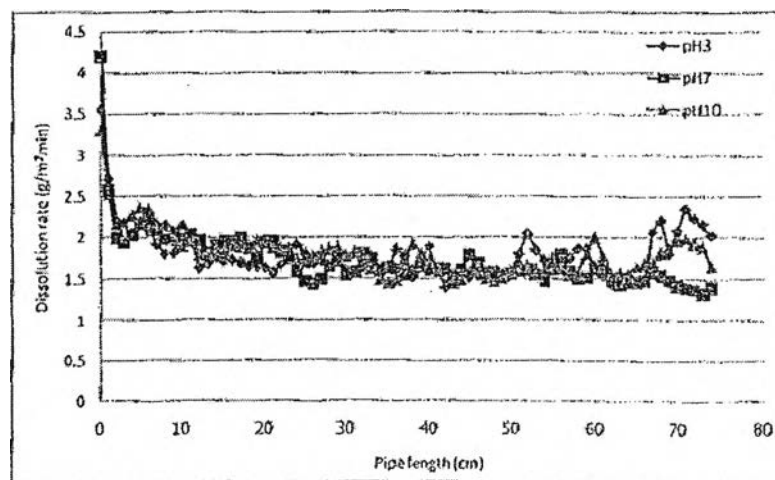


Figure 2.13 Dissolution rate along a plaster of Paris pipe at 25 LPM, 30°C (Warunphaisal, 2009).

2.8.4 The Surface Behavior of Crystal of Gypsum During Dissolution

Fan and Teng (2007) observed the surface behavior of gypsum in undersaturated conditions during mineral dissolution process. In each experiment, aqueous solutions were injected to fluid cell to react with the surface. The surfaces were observed by optical microscope. The step directions $[001]$ and $[100]$ were determined from measure angles that trace moving step. The characteristic of etch pit represent a well-defined parallelogram elongated noticeably in one direction (Figure 2.14).

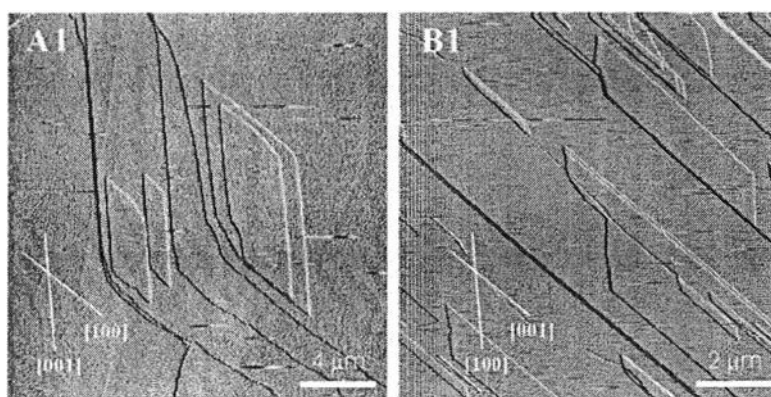


Figure 2.14 Etch pits formed on gypsum (010)-A (A1) and (010)-B (B1) surfaces. Note that the morphologies of the pits in (A1) and (B1) are mirror images of each other (Fan and Teng, 2007).

2.9 **Trans-Cinnamic Acid Characteristics**

Cinnamic acid is a white crystalline organic acid. It is obtained from oil of cinnamon, from balsams such as storax and shea butter. Cinnamic acid is freely soluble in benzene, diethyl ether, acetone, and acetic acid and slightly soluble in water. Cinnamic acid is used in flavors, synthetic indigo, perfume industry and certain pharmaceuticals. Cinnamic's more volatile ethyl esters (ethyl cinnamate) are flavor components in the essential oil of cinnamon, in which related cinnamaldehyde is the major constituent. Cinnamic acid is also part of the biosynthetic shikimate and phenylpropanoid pathways. Its biosynthesis is performed by action of the enzyme phenylalanine ammonia-lyase (PAL) on phenylalanine, (Budavari, Susan, ed., 1996).

Table 2.3 Physico-chemical characteristics of trans-cinnamic acid (Acros Organics BVBA Inc., 2012, Delgado J. M. P. Q., 2007)

Physical State	Crystalline powder
Color	White to pale yellow
Odor	Faint odor
pH	3-4
Boiling Point	300 °C at 760mmHg
Freezing/Melting Point	131-136 °C
Specific gravity	2.31–2.33
Molecular weight (g/mol)	148.16
Density (g/cm ³)	1.248
Solubility in water at 20°C (g/L)	0.4
Mass diffusivity in water at 20°C (m ² /s)	8.8E-10

2.10 Potassium Bitartrate Characteristics

Potassium bitartrate can also be called potassium hydrogen tartrate (KC₄H₅O₆). It is a natural byproduct of winemaking. Potassium bitartrate can be used in many ways. It is primarily used in commercial food production, household cooking and baking, a laxative for both humans and domestic animals. It is also used in the processing of some metals. This compound is also used to clean brass, copper, aluminum, and other metals. Moreover, it is used in the chemical industry as a raw material for the preparation of other tartrates (BookRags, Inc., 2012).

Table 2.4 Physico-chemical characteristics of potassium bitartrate (Fisher Scientific Company, 2012)

Physical State	Crystalline powder
Color	white - fine
Odor	Odorless
Freezing/Melting Point	230 °C
Molecular weight (g/mol)	188.18
Density (g/cm ³)	1.95
Solubility in water at 20°C (g/L)	6.17
Mass diffusivity in water at 20°C (m ² /s)	1.64E-09

2.11 L-Aspartic Acid Characteristics

Aspartic acid is also known as l-asparaginic acid or l-aminosuccinic acid. It is of paramount importance in the citric acid cycle during which other amino acids are synthesized. It usually is found in sugar cane and molasses. Aspartic acid is the precursor to several amino acids such as methionine, threonine, isoleucine, and lysine. Aspartic acid is one of the materials used to produce artificial sweetener and flavor enhancer, which is made only from the l-isomers of the amino acids. The sweet taste of aspartame comes from the combination of l-aspartic acid and l-phenylalanine. l-aspartic acid also promotes a robust metabolism in the urea cycle and participates in gluconeogenesis. Moreover, l-aspartic acid acts as an excitatory neurotransmitter compound (New World Encyclopedia, 2012).

Table 2.5 Physico-chemical characteristics of l-aspartic acid. (Fisher Scientific Company, 2012, Lin S., 2006)

Physical State	Solid
Color	colorless to white
Odor	odorless
pH	2.5-3.5
Freezing/Melting Point	270 - 271 °C
Molecular weight (g/mol)	133.05
Density (g/cm ³)	1.66
Solubility in water at 20°C (g/L)	4.9
Mass diffusivity in water at 20°C (m ² /s)	9.1E-10

2.11.1 Dissolution of L-Aspartic Acid

Shan et al. (2001) investigated the kinetics of l-aspartic acid dissolution with various temperature and particle size. l-aspartic acid crystals were agitated in water with different speeds. The dissolution rate of l-aspartic acid could be determined from simulation of the change in crystal size distribution (CSD) of monodisperse crystals during dissolution. The result showed that dissolution became slower as the temperature decreased.

Table 2.6 The kinetic parameters determined from dissolution of monodisperse crystals of l-aspartic acid (k : cm min^{-1}) (Shan et al., 2001)

Size, L (μm)	15°C	20°C	30°C	45°C
90	0.61	0.7	1.14	1.89
200	0.59	0.71	1.21	1.84
360	0.58	0.73	1.19	2.01
460	0.66	0.76	1.14	1.96
k_d (average)	0.61 ± 0.03	0.73 ± 0.02	1.17 ± 0.03	1.93 ± 0.06

2.12 Jet Impingement Study

Jet impingement systems are used in many engineering applications such as glass manufacturing and cooling of electrical equipment due to high heat and mass transfer rates. They allow high convective transfer rates between the bulk and the surface by increasing the velocity of fluid impinging onto the surface (Pierrefeu, D. L., 2009).

Jets can be classified in several categories, which are (1) fluid types: submerged and free jets, (2) orientation: oblique and normal jets, (3) nozzle shape: round, slot and elliptic jets, (4) impingement surface: flat and treated surfaces, (5) restriction imposed upon the jet at the jet exit: confined, partially confined and unconfined jets, and (6) number of jets: single and multiple jets (Pekdemir, 1994).

2.12.1 Hydrodynamic Characteristics

Jet impingement is a test technique that may be used to study flow-accelerated corrosion. The flow field has been established for a circular submerged jet impinging on a flat plate. Under these conditions, a stagnation point will exist at the intersection of the jet/nozzle axis with the plate, and the flow will be symmetric about the axis (Efird et al., 1993). The characteristic flow regions are shown in Figure 2.15.

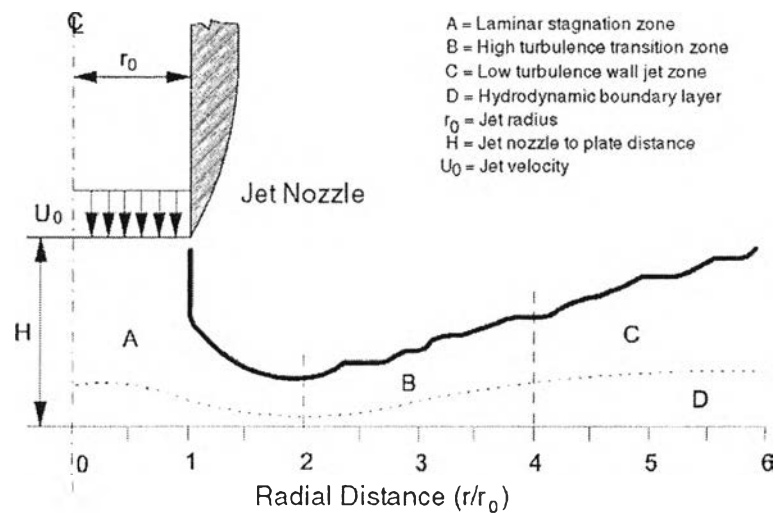


Figure 2.15 Hydrodynamic characteristics of jet impingement on a flat plate showing the four characteristic flow regions (Efird et al., 1993).

Region A is the stagnation zone. The flow is laminar and produces a high pressure region up to $r/r_0 = 2$. Region A extends from the central axis to the point of maximum velocity and minimum jet thickness. Because the flow vector changes rapidly as radial distance increases, this region is defined poorly on the basis of wall shear stress.

Region B is a zone of rapidly increasing turbulence, with the flow developing into a wall jet. This region starts between $r/r_0 = 2$ and $r/r_0 = 4$. The flow pattern is characterized by high wall shear stress, a large velocity gradient at the wall, and high turbulence. Region B is of primary interest for studying fluid flow effects on corrosion in high-turbulence areas.

In the flow pattern of Region C, the bulk flow rate and turbulence decay rapidly as the thickness of the wall jet increases, momentum is transferred away from the plate and the surrounding fluid is entrained. This region is amenable to mathematical characterization (Efird et al., 1993).

2.12.2 Mass Transfer

For jet impingement systems, mass transfer correlations have been derived by various researchers. The mass transfer can be represented by the Sherwood number (Sh), which depends on the Reynolds (Re) and Schmidt (Sc)

numbers, the relative jet length (H/d_0) and the relative radial distance from the stagnant point (r/d_0). The Reynolds and Nozzle number (nozzle size) are based on the nozzle exit diameter and average velocity if not specified otherwise. From equation 2.15, the mass transfer coefficient can be deduced from the Sherwood number:

$$\text{Sh} = \frac{kd_0}{D_{AW}^\circ} \quad (2.15)$$

where k is the mass transfer coefficient (m/s), d_0 is the nozzle diameter (m) and D_{AW}° is the diffusivity of species A in water (m^2/s).

Sherwood number equations from many literature sources are summarized in Table 2.7.

Table 2.7 Summary of Sherwood number equations (Pierrefeu, D. L., 2009)

Author	Investigation	Sh equation	Re	H/d ₀	r/d ₀
Chin and Tsang, 1978	Mass transfer from impinging jet to a circular disk.	$Sh = 1.12Re^{0.5}Sc^{0.33}(H/d_0)^{-0.057}$	4,000 to 16,000	0.2 to 6	0.1 to 1
Rao and Trass, 1964	Mass transfer from water jet impinging on flat surface coated with trans-cinnamic acid.	$Sh = 1.3Re^{0.84}(r/d_0)^{-1.27}$ for Sc = 900	20,000 to 125,000	0.2 to 19	>4.5
				Average Sherwood number within the stagnation and transition region.	$Sh = 0.046Re^{1.06}(H/d_0)^{-0.09}$
		$Sh = 0.107Re^{1.06}(H/d_0)^{-0.54}$		>6.5	

Table 2.7 (Cont'd) Summary of Sherwood number equations (Pierrefeu, D. L., 2009)

Author	Investigation	Sh equation	Re	H/d ₀	r/d ₀
Chin and Hsueh, 1986	Mass transfer from an unsubmerged circular jet to flat surface.	$Sh = 0.9Re^{0.5}Sc^{0.33}(H/d_0)^{-0.09}$	2,500	0.5	<0.8
		$Sh = 0.77Re^{0.5}Sc^{0.33}(r/d_0)^{-0.5}$	to 20,000	to 5	0.8 to 4
Arzutug et al., 2005	Mass transfer from conventional impinging jet	$Sh_{mean} = 0.03Re^{0.66}Sc^{0.33}(H/d_0)^{-0.03}$ $Sh_{max} = 1.97Re^{0.38}Sc^{0.33}(H/d_0)^{-0.04}$	10,950 to 50,800	2	4

*** All the studies were performed at 25 °C.